# Multiple-shell structures of laser-cooled $^{24}Mg^+$ ions in a quadrupole storage ring

**G. Birkl, S. Kassner & H. Walther**

Max-Planck-Institut für Quantenoptik, Garching bei München, Germany

**THE possibility of creating ordered ion beams in high-energy storage rings[1,2] by means of electron and laser cooling has opened up a new era in accelerator physics. The enhanced luminosity and suppressed momentum spread in such systems create the highest possible phase-space density. The first experimental results were obtained by cooling $^7Li^+$ beams to temperatures of a few kelvin or even to sub-kelvin temperatures[3,4], and the ordered structures have been studied theoretically[5–7] by methods of molecular dynamics. Predicted configurations for the lowest ion densities have been observed in low-energy quadrupole storage rings[8] and linear traps[9]. Recently we showed that at slightly higher ion densities helical structures are obtained[10]. Here we present a series of new experimental results on ordered ion structures in a quadrupole storage ring. In order of increasing ion number, a linear chain of ions, a zig-zag structure, helical structures and finally multiple concentric shells could be observed. The experimental results agree with molecular dynamics calculations.**

When ordered structures in storage rings are simulated[5–7], a cylindrically symmetric, static harmonic potential is usually assumed to describe the confining field. The pseudopotential of a low-energy quadrupole storage ring is closer to the theoretical model than the confining field of a high-energy storage ring, where the ions are subjected to periodic squeezing and pulling in the focusing sections, Coulomb explosion in the drift sections and shear forces in the bending sections. The principle and first realizations of quadrupole storage rings are described in refs 11–13. In the ring the ions can move freely along the axis of the quadrupole field and are radially confined by applying a radiofrequency (r.f.) voltage $U_{RF}\cos\Omega t$ to the electrodes. This leads to a harmonic confining potential[14] of the form $\psi = \psi_0 r^2/r_0^2$ with the potential depth $\psi_0 = q^2U_{RF}^2/4m\Omega^2r_0^2$, where $q$ is the ion charge, $m$ the ion mass, $r$ the distance from the field axis and $r_0$ half the distance between opposite electrodes. The oscillation frequency in this harmonic potential, $\omega_{sec} = (2\psi_0/mr_0^2)^{1/2}$, is called the secular frequency[14]. Ions in a r.f. quadrupole field also show micromotion with frequency $\Omega$, the amplitude of which increases in proportion to the distance $r$ from the field axis. To compare experimental results with theory, it is useful to define the normalized 'linear particle density'[7], $\lambda = aN/2\pi R$. Here $N$ is the total number of stored ions in the ring, $R$ the ring radius and $a$ the Wigner–Seitz radius, $a = (3q/8\pi\varepsilon_0 K)^{1/3}$, where $K$ is the force constant. For the ring trap, $K = 2\psi_0/qr_0^2$, which leads to $a = (3q^2r_0^2/16\pi\varepsilon_0\psi_0)^{1/3}$. The quantity $a^3$ corresponds to the volume of the unit cell of the Coulomb crystal. The equilibrium structures resulting from the molecular dynamics (MD) calculations as a function of increasing $\lambda$ are a linear chain, a zig-zag, a single shell and multiple shells[5–7]. For the single shell, different ion configurations on the shell surface, such as single and multiple helices, have also been calculated in detail[6,7]. Static properties of these configurations, such as shell diameters and the arrangement of the ions on the shell surfaces, can also be obtained by minimizing the energy in an electrostatic model[7,15].

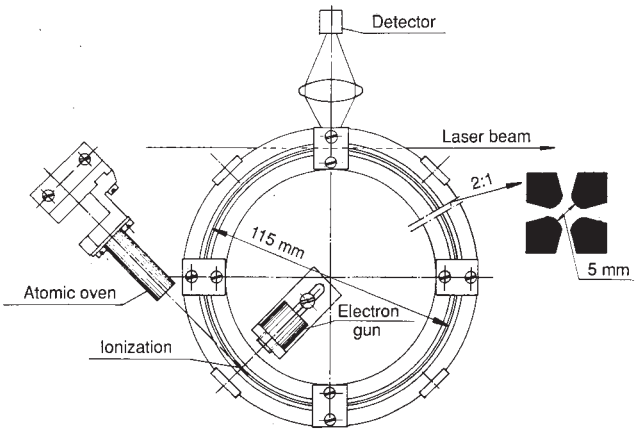


FIG. 1 Quadrupole storage ring, with the atomic beam oven and electron gun. The storage ring consists of four circular electrodes, and the diameter of the toroidal storage volume is $2R = 115$ mm. The insert shows an enlarged cross-section with opposite electrodes having a separation of $2r_0 = 5$ mm. The laser beam enters the storage volume tangentially. Resonance fluorescence is detected with a photomultiplier tube or an imaging photon detector system.

Figure 1 shows the quadrupole storage ring. The toroidal trap volume has a diameter $2R = 115$ mm, and the distance between opposite electrodes is $2r_0 = 5$ mm. The radiofrequency is $\Omega = 2\pi \times 6.56$ MHz, and the secular frequency $\omega_{sec}$ is of the order of megahertz. The geometry of the quadrupole and measurement of the r.f. voltage allow the potential depth to be determined with an accuracy of 5%. The apparatus is contained in an ultra-high-vacuum chamber with a pressure below $10^{-8}$ Pa. Magnesium ions $^{24}Mg^+$ are created by electron bombardment of a thermal atomic beam. A contact potential barrier of ~1 eV is produced by deposition of stray magnesium atoms on the electrodes in the region where the atomic beam passes through the quadrupole. The potential barrier enables us to cool the stored ions to rest, using only a single laser beam[10]. Laser light with a wavelength of 280 nm, resonant with the $3^2S_{1/2}$–$3^2P_{3/2}$ transition of $^{24}Mg^+$, is focused tangentially along the axis of the quadrupole field, where it can interact with the stored ions. The resonance line of $^{24}Mg^+$ can easily be saturated with the available laser power of several milliwatts. The fluorescence light emitted by the ions is measured by a photomultiplier tube and an imaging photon detector system equipped with a two-stage microchannel plate and a position analyser, the channel diameter being 25 μm. The lens system used for the optical imaging has a focal length of 35 mm and allows the image of the ion structure to be magnified between 10 and 70 times. For most of the measurements a magnification factor of 40 was used. Thus the imaging system allows a resolution of ~1 μm in the storage volume. The diffraction-limited resolution of the optics is 0.4 μm.

Previous work has shown[8,10] that laser Doppler cooling of the stored $Mg^+$ ions leads to a phase transition from a disordered state to an ordered crystalline structure with the same features as described for ions stored in a Paul trap[16,17]. In contrast to high-energy storage rings, in the quadrupole ring the laser-cooled ions are at rest, and therefore the structures can be investigated in detail. Ordered ion configurations have also been observed in Paul[16–18] and Penning[19] traps.

Figure 2 shows ordered structures for low ion densities, leading to images of singly resolved ions. The ion spacings are known to an accuracy of 3%, and therefore the ion density can be directly determined from the images with the same error. The $\lambda$ parameters can be calculated with 5% accuracy for these structures. A linear chain of ions with an ion spacing of 33 μm is presented in Fig. 2*a*. Increasing the ion density favours configurations in which the ions are displaced from the field axis, leading to a zig-zag structure (Fig. 2*b*). The ions are arranged in a plane perpendicular to the direction of observation, as can be concluded from their spacing (26 μm in the direction of the field axis) and the potential depth. Further increasing the ion density changes the equilibrium configuration into helical structures. The experimental image in Fig. 2*c* shows an ordered structure which can be described as two interwoven

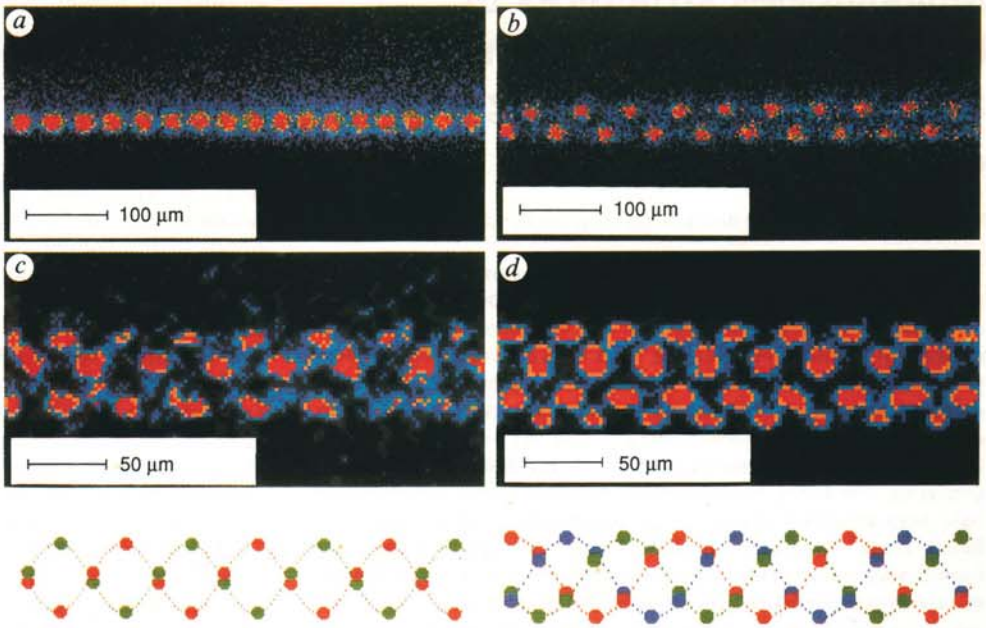


FIG. 2 Colour-coded images of crystalline structures of laser-cooled $^{24}Mg^{+}$ ions. The intensity increases from violet to blue, yellow and red. Individual ions could be resolved in these images. The ions arrange themselves in minimum energy configurations. *a*, For low ion density ($\lambda = 0.29$) the ions form a string along the field axis; *b*, increasing the ion density changes the configuration to a zig-zag ($\lambda = 0.92$). At still higher ion densities the ions form ordered helical structures on the surface of a cylinder: *c*, two interwoven helices at $\lambda = 1.9$; *d*, three interwoven helices at $\lambda = 2.6$. Experimental images are displayed above, visualizations below.

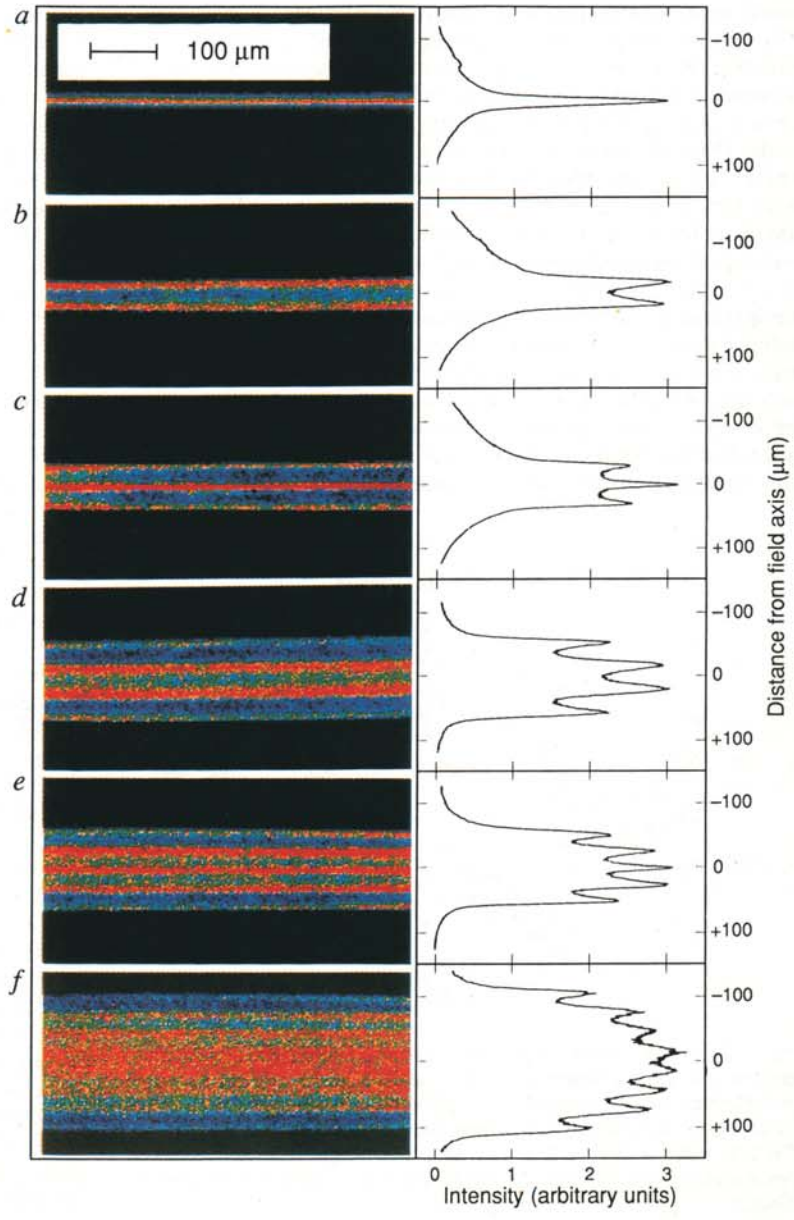


FIG. 3 Images and intensity profiles of (*a*) string, (*b*) one shell ($\rho/a = 1.05$, total ion number in the ring $N \approx 5 \times 10^4$), (*c*) one shell plus string ($\rho/a = 1.8$, $N \approx 1 \times 10^5$), (*d*) two shells ($\rho/a = 2.7$, $N \approx 2 \times 10^5$), (*e*) two shells plus string ($\rho/a = 3.4$, $N \approx 3 \times 10^5$) and (*f*) four shells ($\rho/a = 6.2$, $N \approx 8 \times 10^5$). The ions are not individually resolved. The structures can be identified with the help of the radial intensity profiles (right). The images are colour-coded as in Fig. 2. Integration times are longer than 3 min each.

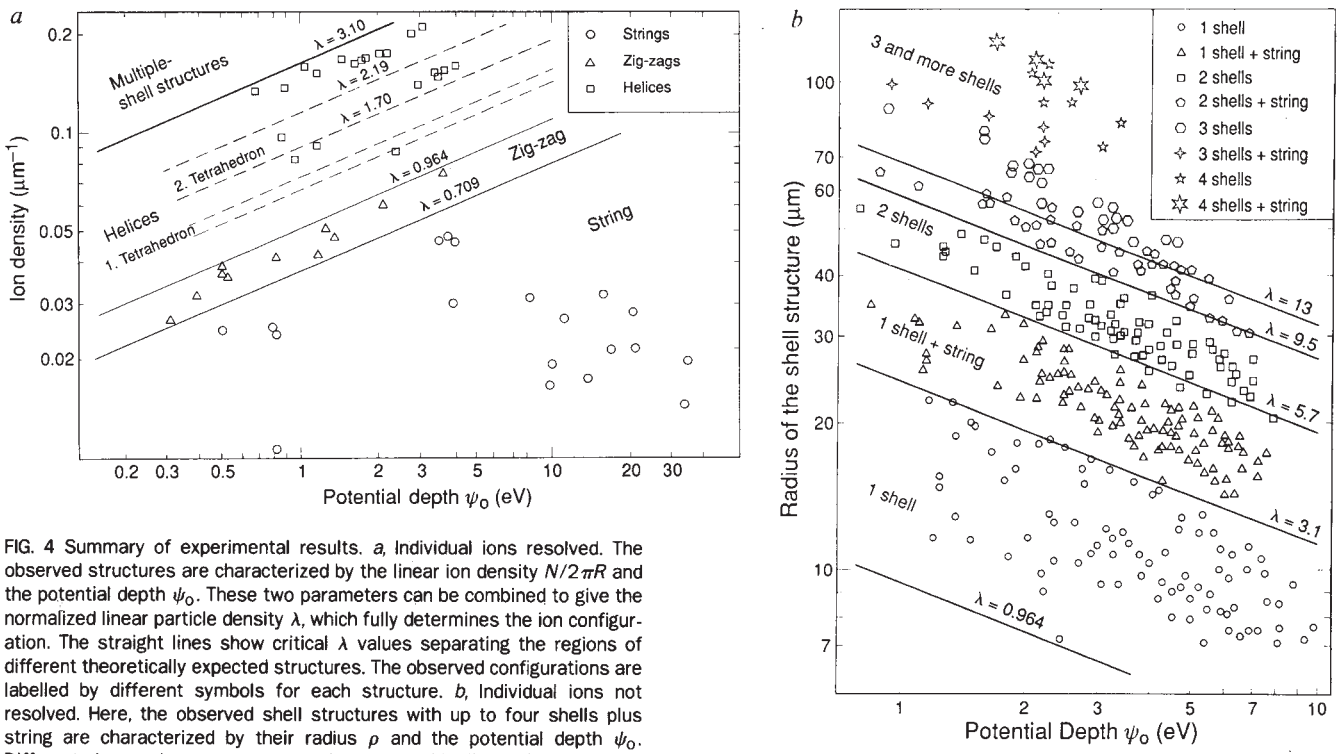


FIG. 4 Summary of experimental results. *a*, Individual ions resolved. The observed structures are characterized by the linear ion density $N/2\pi R$ and the potential depth $\psi_0$. These two parameters can be combined to give the normalized linear particle density $\lambda$, which fully determines the ion configuration. The straight lines show critical $\lambda$ values separating the regions of different theoretically expected structures. The observed configurations are labelled by different symbols for each structure. *b*, Individual ions not resolved. Here, the observed shell structures with up to four shells plus string are characterized by their radius $\rho$ and the potential depth $\psi_0$. Different observed structures are again separated by lines of theoretically determined critical $\lambda$.

helices with a diameter of 44 μm and four ions per pitch. The image in Fig. 2*d*, recorded with an even higher ion density, shows a structure of three interwoven helices with a diameter of 53 μm and six ions per pitch. The fact that the structures in Fig. 2*b* to *d* do not rotate around the field axis shows that there must be small deviations from the rotational symmetry around the quadrupole axis, which may be caused by the contact potential or a misalignment of the trap electrodes. By increasing the radiation pressure the structures can be slightly compressed in the direction of the incoming laser beam. As mentioned above, the contact potential prevents the structures from starting to rotate around the ring.

Increasing the ion number and the potential depth accordingly leads to identical structures, but with smaller ion spacings, so that the ions can no longer be individually resolved (Fig. 3). Information about the structures can be extracted from the radial intensity profiles, giving a measure of the ion distribution in this direction. Instead of the parameter $\lambda$, it is now possible to use the radius $\rho$ of the structure in units of the Wigner–Seitz radius $a$ (where $a$ is determined by the potential depth) to characterize the structures. The zig-zag and helix both produce a double-peak structure in the radial intensity profile (Fig. 3*b*). If, therefore, the ion density is so high that observation of individual ions is not possible, we cannot discriminate between the zig-zag and helical structures. This is only true because we are looking perpendicularly to the plane of the zig-zag, as in Fig. 2*b*. Successively increasing the ion density or lowering the potential leads to the occurrence of a string inside the shell (Fig. 3*c*), two concentric shells (Fig. 3*d*) and two shells plus string (Fig. 3*e*). Figure 3*f* shows a four-shell structure for very high densities. We have observed all possible shell structures up to four shells plus string. All these structures form after a phase transition from a disordered state, indicating that the ions occupy fixed positions within the shells. This differs from the observations of shell structures in a Penning trap[19]. The structures in Figs 2*b–d* and 3*b–f* are not free of micromotion, but the amplitude of this motion is too small to be observable at the present optical resolution.

The intensity profiles of Fig. 3 show decreasing contrast for a higher number of shells. This is partly due to the summation of the intensity distributions of more and more shells in a multiple-shell configuration, which masks the individual structures. In addition, for higher-order structures the inner shells become substantially thicker, as pointed out in ref. 7. Our experiments show that it is possible to obtain ordered configurations even for very high ion densities.

Figure 4*a* gives a summary of experimental data for all recorded images in which the ions were individually resolved. The potential depth $\psi_0$ and linear ion density $N/2\pi R$ (obtained directly from the images with the known optical magnification) are the experimental parameters. The theoretical limits[7] between the different structures are given by the straight lines with constant $\lambda$. String structures are expected for $\lambda < 0.709$, zig-zag structures in the range $0.709 < \lambda < 0.964$ and single shells in the range $0.964 < \lambda < 3.10$. In the single-shell regime, many different structures are expected that are practically degenerate in energy. The structures may change on a timescale short compared with the averaging time of the imaging system, owing to their residual thermal energy. For that reason it is difficult to obtain clear images in much of this $\lambda$ regime. The stability could be improved by cooling the ions further. We obtained stable configurations for several seconds (more than $10^5$ secular periods of the system) near $\lambda = 1.3$ and $\lambda = 2.0$, yielding structures of two interwoven helices (Fig. 2*c*) and near $\lambda = 3.0$ structures of three interwoven helices (Fig. 2*d*). The two-fold helix is also expected from the MD calculations, the structure forming a series of tetrahedra[7]. The expected $\lambda$ domains for this configuration are marked by the dashed lines in Fig. 4*a*. For a large range of experimental parameters the observed structures fit into the expected scheme, confirming the theoretical results. Thus the kind of structures observed is fully determined by $\lambda$, which proves to be a universal parameter independent of the experimental conditions.

Figure 4*b* summarizes the experimental results on the ordered shell structures up to four shells plus string without resolution of individual ions. Again the potential depth $\psi_0$ is one of the experimental parameters. As the ion density can no longer be determined directly from the images, the radius $\rho$ of the structures is used instead as the second parameter. The theoretical limits between the different shell structures are again given as straight lines with constant $\lambda$, as predicted in ref. 7, where the functional dependence of $\rho/a$ on $\lambda$ is established. The observed ion configurations are fully determined by $\rho/a$ and therefore by $\lambda$ for a variety of potential depths and ion densities. □

Received 7 February; accepted 14 April 1992.

1. Schiffer, J. P. & Kienle, P. *Z. Phys.* A**321,** 181 (1985).
2. *Proc. Workshop on Crystalline Ion Beams* (eds Hasse, R. W. Hofmann, I. & Liesen, D.) 2–63 (GSI, Darmstadt, 1989).
3. Schröder, S. *et al. Phys. Rev. Lett.* **64,** 2901–2904 (1990).
4. Hangst, J. S. *et al. Phys. Rev. Lett.* **67,** 1238–1241 (1991).
5. Rahmän, A. & Schiffer, J. P. *Phys. Rev. Lett.* **57,** 1133–1136 (1986).
6. Habs, D. in *Lecture Notes in Physics 296: Frontiers of Particle Beams* (Springer, New York, 1988).
7. Hasse, R. W. & Schiffer, J. P. *Ann. Phys.* **203,** 419–448 (1990).
8. Walther, H. in *Proc. Workshop on Light Induced Kinetic Effects on Atoms, Ions and Molecules* (eds Moi, L., Gozzini, S., Gabbanini, C. Arimondo, E. & Strumia, F.) 261–276 (ETS Editrice, Pisa, 1991).
9. Raizen, M. G., Gilligan, J. M., Bergquist, J. C., Itano, W. M. & Wineland, D. J. *J. mod. Opt.* **39,** 233–242 (1992).
10. Waki, I., Kassner, S., Birkl, G. & Walther, H. *Phys. Rev. Lett.* **68,** 2007–2010 (1992).
11. Drees, J. & Paul, W. *Z. Phys.* **180,** 340–361 (1964).
12. Church, D. A. *J. appl. Phys.* **40,** 3127–3134 (1969).
13. Deutch, B. I. *et al. Phys. Script.* T**22,** 248–255 (1988).
14. Dehmelt, H. in *Advances in Atomic and Molecular Physics* Vol. 3, 53–72 (Academic, New York, 1967).
15. Totsuji, H. & Barrat, J.-L. *Phys. Rev. Lett.* **60,** 2484–2487 (1988).
16. Diedrich, F., Peik, E., Chen, J. M., Quint, W. & Walther, H. *Phys. Rev. Lett.* **59,** 2931–2934 (1987).
17. Blümel, R. *et al. Nature* **334,** 309–313 (1988).
18. Wineland, D. J., Bergquist, J. C., Itano, W. M., Bollinger, J. J. & Manney, C. H. *Phys. Rev. Lett.* **59,** 2935–2938 (1987).
19. Gilbert, S. L., Bollinger, J. J. & Wineland, D. J. *Phys. Rev. Lett.* **60,** 2022–2025 (1988).

ACKNOWLEDGEMENTS. We thank C. A. Schrama for discussions.